Hard superconducting gap and diffusion-induced superconductors in Ge-Si nanowires

Joost Ridderbos,[1] Matthias Brauns,[1] Jie Shen,[2] Folkert K. de Vries,[2] Ang Li,[3] Sebastian Kölling,[3] Marcel A. Verheijen,[3] Alexander Brinkman,[1] Wilfred G. van der Wiel,[1] Erik P. A. M. Bakkers,[3] and Floris A. Zwanenburg[1,*]

[1] *MESA+ Institute for Nanotechnology, University of Twente, P.O. Box 217, 7500 AE Enschede, The Netherlands*

[2] *QuTech and Kavli Institute of Nanoscience, Delft University of Technology, 2600 GA Delft, The Netherlands*

[3] *Department of Applied Physics, Eindhoven University of Technology, Postbox 513, 5600 MB Eindhoven, The Netherlands*

(Dated: January 30, 2022)

We show a hard superconducting gap in a Ge-Si nanowire Josephson transistor up to in-plane magnetic fields of 250 mT, an important step towards creating and detecting Majorana zero modes in this system. A hard gap requires a highly homogeneous tunneling heterointerface between the superconducting contacts and the semiconducting nanowire. This is realized by annealing devices at 180 °C during which aluminium inter-diffuses and replaces the germanium in a section of the nanowire. Next to Al, we find a superconductor with lower critical temperature (T_C = 0.9 K) and a higher critical field (B_C = 0.9 − 1.2 T). We can therefore selectively switch either superconductor to the normal state by tuning the temperature and the magnetic field and observe that the additional superconductor induces a proximity supercurrent in the semiconducting part of the nanowire even when the Al is in the normal state. In another device where the diffusion of Al rendered the nanowire completely metallic, a superconductor with a much higher critical temperature (T_C = 2.9 K) and critical field (B_C = 3.4 T) is found. The small size of these diffusion-induced superconductors inside nanowires may be of special interest for applications requiring high magnetic fields in arbitrary direction.

INTRODUCTION

The discovery that Majorana fermions offer a route towards an inherently topologically protected fault-tolerant quantum computer [1–3] marked the beginning of a quickly growing field of research to achieve their experimental realization. Majorana fermions require a topological superconducting material, which in practice can be realized by coupling a conventional *s*-wave superconductor to a 1-dimensional nanowire with high spin-orbit coupling and *g*-factor [4–7]. Signatures of Majorana fermions are expected to arise as a conductance peak at zero bias and finite magnetic fields. The first reports showing these zero-bias conductance peaks in InAs and InSb nanowires [8–14] suffered from sizeable sub-gap conductivity attributed to inhomogeneities in the nanowire-superconductor interface [15, 16]. The resulting quasiparticle poisoning decoheres Majorana states since they will participate in braiding operations [17–19], and additionally obscure the Majorana signatures at zero energy. Strong efforts have been made to improve these interfaces, i. e., induce a hard gap, using epitaxially grown Al [20, 21] or specialized surface treatments methods [22, 23], resulting in a much better resolved Majorana signatures [18, 24–26].

In contrast to the group III-V materials used in most previous work, we use Ge-Si core-shell nanowires consisting of a mono-crystalline Ge ⟨110⟩ core with a diameter of ∼15 nm, and a Si shell thickness of 2.5 nm covered by a native SiO_2. Coherent strain in the defect-free crystal structure results in high hole-mobilities [27]. The electronic properties of the one-dimensional hole gas localized in the Ge core [28, 29] makes them a candidate for observing Majorana fermions [30, 31], and their interaction with a superconductor is still relatively unexplored [32–36]. These wires are predicted to have a strong first-order Rashba type spin-orbit coupling [37] which, together with the *g*-factor [38, 39], is tunable by electric fields. Our devices consist of a nanowire channel with superconducting Al source and drain placed on an oxidized Si substrate (for more detailed information about the fabrication process see Supplementary Information SI 1). We focus on two devices where an essential thermal annealing process results in inter-diffusion between Al in the contacts and Ge in the nanowire channel. Device A is an electric-field tunable Josephson junction [34, 36] as shown in Fig. 1a, while in device B the whole semiconducting nanowire channel has been metalized and we suspect Al has largely replaced the semiconductor.

The electric field dependence of Device A has already been extensively studied in Ref. [34], where the main result was the observation of two distinct regimes: a highly transparect regime with a near ideal $I_C R_N$ product in accumulation, and a tunneling regime with few-hole occupancy where supercurrent only appears at the charge degeneracy points. In this work, we extend on this by investigating the magnetic field dependence of the transport properties in both regimes.

To gain insight into the microscopic properties of the superconductor-semiconductor interfaces, we start by investigating Device A using high-angle annular dark field (HAADF) - scanning transmission electron microscopy (STEM) in combination with energy-dispersive X-ray

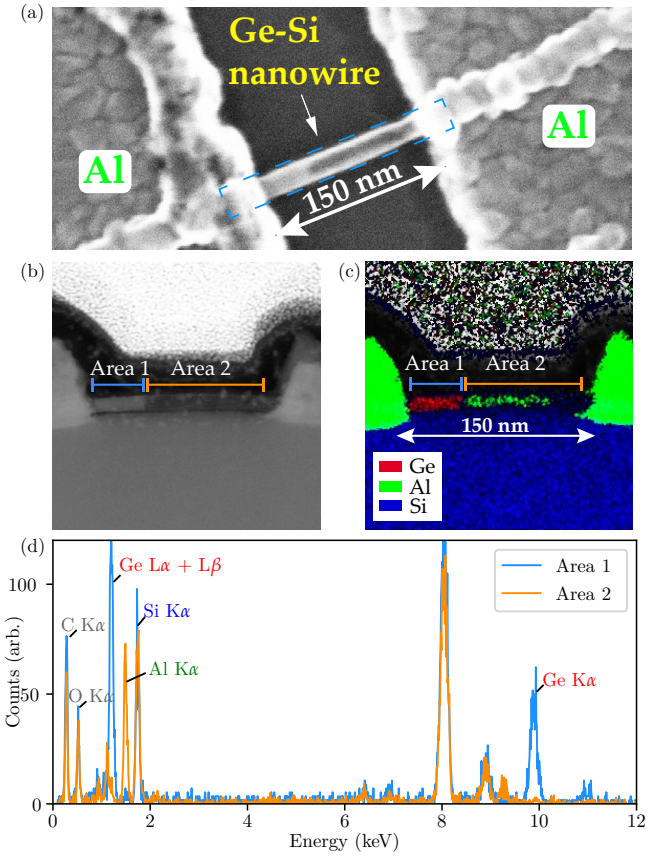

FIG. 1. **Al-Ge inter-diffusion in device A:** a) Top view SEM image of the device showing a Ge-Si nanowire between two Al contacts. In the right part of the nanowire, a slightly darker contrast is observed (see Supplementary Info Fig. 2 for SEM images showing this effect in several devices). The blue dashed line shows the approximate location of the TEM lamella. b) Cross-sectional HAADF-STEM image of the same device. The same contrast difference as in a) is observed. c) HAADF/STEM image with combined EDX data for elements Ge, Al and Si (see Supplementary Info Fig. S1 for separate images). d) EDX spectrum for Area 1 and Area 2 as defined in c).

spectroscopy (EDX). We find strong indications that the additional superconductor, as well as the highly homogeneous superconductor-nanowire interface arises during the thermal annealing process where Al inter-diffuses with the material in the semiconducting nanowire. In the second part, we map the switching current I_{SW} as a function of critical field B_C and critical temperature T_C of device A and B, which clearly shows an additional superconducting phase in both devices. In the final part we investigate the hardness of the superconducting gap in the semiconducting nanowire of device A, by means of electronic transport measurements near depletion [20, 23] and observe that the conductance in the gap is suppressed by a factor ~ 1000.

AL-GE INTER-DIFFUSION

To investigate the effects of the annealing on the stoichiometric composition of the nanowire channel, a TEM lamella was made along the nanowire axes of device A as indicated in Figure 1a. We first apply a stack of protective SiO_2 and Pt layers and subsequently create the TEM lamella using a standard focused ion beam lift-out protocol. This allows us to perform an analysis on the cross-section of the device as can be seen in Fig. 1b. In both Fig. 1a and b, a smaller region (Area 1) with higher contrast on the left, and a bigger region with lower contrast on the right (Area 2) can be observed. Fig. 1c shows the resulting EDX signals in these regions for the elements Ge, Si and Al and we observe a clear distinction: in Area 1 we observe a strong Ge signal while in Area 2 the signal is dominated by Al.

In Figure 1d we show the integrated EDX spectra for both areas. When comparing the two areas, we observe that in Area 2 the Ge $L\alpha$, Ge $L\beta$ and Ge $K\alpha$ signals fall below the detection limit. As is the convention in EDX analysis, L and K denote the orbital to which an electron decays in a picture where K, L, and M are the outer atomic orbitals, while α and β indicate whether it decays from the first or second higher orbital. The Al $K\alpha$ signal shows the opposite behavior, implying that Ge has been replaced by Al in Area 2. The counts for elements O, C and Si remain equal in both areas (see also Supplementary Information Fig. S1). As we will discuss in the following section, the superconductor in Area 2 has profoundly different properties from the Al contacts and we therefore refer to it as X1. Inter-diffusion has also taken place below the left contact without reaching the channel, although this is not evident from the TEM data. Instead, we conclude this from transport data in the next section (Fig. 2 and Supplementary Information Fig. S3). As a side-note, we cannot observe the effects of the inter-diffusion process on the Si shell, since the Si signal is dominated by the SiO_2 that covers the substrate.

An in-depth study on the thermally induced inter-diffusion process between Al and pure Ge $\langle 111 \rangle$ nanowires, a highly similar system to ours, has been performed in Refs. 40, 41. Here, in-situ monitoring of the metal front inside the nanowires at various temperatures reveals that the velocity of propagation as a function of the length of the metalized nanowire segment, is volume-diffusion limited, and possibly surface-diffusion limited, with the Al forming a mono-crystalline face-centered-cubic crystal inside the nanowire. The metal front forms an atomically sharp interface and no inter-metallic phase is found in the metalized nanowire segment, i.e., the Ge is transported out of the wire into the Al contacts. These observations are explained by a 15 orders of magnitude lower diffusion constant for Al in Ge than for Ge in Al [42, 43]. Furthermore, the initial start of the dif-

fusion reaction is governed by the respective activation energies (121.3 kJ/mol for Ge in Al, 332.8 kJ/mol Al in Ge [42, 43]) and may depend on the specific atomic arrangement of the initial nanowire-Al interface, explaining the variation in the starting time of the diffusion reaction, even for two separate contacts on the same wire. These findings largely correspond to our observations on Ge-Si core-shell nanowires and gives an explanation for the asymmetry in our contacts (see Supplementary Figure S2 for SEM images of partly and fully metalized nanowires) , as well as the variation in device properties.

TWO SUPERCONDUCTORS IN A NANOWIRE JOSEPHSON JUNCTION

In Fig. 2a we show a magneto-spectroscopy of device A, the Josephson junction: we plot the differential resistance $\partial V_{\mathrm{SD}}/\partial I_{\mathrm{S}}$ versus the sourced current I_{S} and the out-of-plane magnetic field $B_{\perp}$ (see illustration in Fig. 3b) while sweeping I_{S} from negative to positive current. The backgate V_{BG} is fixed at -4.7 V where multiple subbands contribute to transport and the junction is highly transparent [34]. The superconducting region (black) is bounded by $I_{\mathrm{R}} < I_{\mathrm{S}} < I_{\mathrm{SW}}$ with I_{R} the retrapping current at negative bias and I_{SW} the switching current at positive bias. Upon increasing $B_{\perp}$ from 0, I_{SW} decreases gradually until aluminum becomes normal at the critical out-of-plane field $B_{\mathrm{C}\perp,\mathrm{Al}} \approx 40$ mT after which a finite I_{SW} remains. For all $B_{\perp}$, $I_{\mathrm{SW}} > I_{\mathrm{R}}$ indicating that our junction is hysteretic for this particular value of V_{BG} due to the junction being underdamped [34] while additional heating-induced hysteresis can not be excluded [44] (see Supplementary Information Fig. S3a for a gate-dependence of I_{SW} and I_{R}).

When increasing $B_{\perp}$ further in Fig. 3b, I_{SW} slowly decreases and finally disappears. The proximity-induced supercurrent above $\left|B_{\mathrm{C}\perp,\mathrm{Al}}\right|$ implies the presence of a second superconducting material, X1, in or near the nanowire channel with a critical field $B_{\mathrm{C}\perp,\mathrm{X1}} \approx 950$ mT. To confirm that our Al contacts are normal for $B_{\perp} > \left|B_{\mathrm{C}\perp,\mathrm{Al}}\right|$, we consider the background resistance R_{B} in the superconducting region as a function of $B_{\perp}$ in the bottom panel of Fig. 2b. $R_{\mathrm{B}} = 0$ for $B_{\perp} < \left|B_{\mathrm{C}\perp,\mathrm{Al}}\right|$, while for $B_{\perp} > \left|B_{\mathrm{C}\perp,\mathrm{Al}}\right|$ the background resistance gradually increases to $R_{\mathrm{B}} \approx 0.25$ kΩ attributed to a normal series resistance of the Al contacts. Additionally, the out-of-plane critical field of a separately measured Al lead matches $B_{\mathrm{C}\perp,\mathrm{Al}}$ (see Supplementary Information Fig. S4).

In Fig 2c we show a magneto-spectroscopy at 900 mK and observe that X1 is quenched for all $B_{\perp}$, while Al still induces a supercurrent for $B_{\perp} < |25|$ mT. This shows that X1 has a lower T_{C} and a higher B_{C} than the Al contacts. Because X1 has a higher B_{C} and a lower T_{C} than Al, we can selectively switch either superconductor to the normal state, resulting in four possible device configurations **I-IV** as illustrated in Fig. 2 and summarized in the inset in Fig. 2d (a precise set of conditions for each configuration can be found in Supplementary Information Table S1). Fig. 2d shows plots of V_{SD} versus I_{S} in all four configurations, clearly showing a supercurrent in configuration **II** where Al is normal and only X1 is superconducting. Since we observe a gate-tunable Josephson current even in configuration **II**, we conclude X1 is present on both sides of the Ge-Si segment (see Supplementary Information Fig. S3 for differential resistance maps versus backgate in all four configurations).

JUNCTION I_{SW} VERSUS B AND T

For the observed superconductors and their specific geometries, the critical field and critical temperature are inter-dependent variables and may have a non-trivial relation, the boundaries of the configurations **I-IV** in terms of B_{C} and T_{C} cannot directly be deduced from the data in Fig. 2. We therefore collect I_{SW} versus B from magneto-spectroscopies for a large number of temperatures and the three main magnetic field axes $B_{\star}$, $B_{\perp}$ and $B_{\parallel}$ which are illustrated by the inset in Fig. 3b. For the in-plane field perpendicular to the nanowire, I_{SW} has two clearly distinct overlapping shapes as a function of T and $B_{\star}$ in Fig. 3a: The 'peak' extending to $T \approx 1400$ mK at $B = 0$ with a width of $|B_{\star}| \approx 250$ mT at $T = 50$ mK is attributed to the superconducting state of Al, while the second shape (the 'tail'), extending up to ~ 1000 mT at $T = 50$ mK, corresponds to the superconducting phase of X1. We can thus map the four configurations in the color plot on the T vs $B_{\star}$ axes.

We now extract both the T_{C}-$B_{\mathrm{C}\star,\mathrm{Al}}$ and T_{C}-$B_{\mathrm{C}\star,\mathrm{X1}}$ curves from Fig. 3a (see Supplementary Information section SII), i. e., the critical temperature - critical field relation for Al and X1, and plot them in Fig. 3b. We perform the same procedure for field directions $B_{\perp}$ and $B_{\parallel}$ (see Supplementary Information Fig. S5 for I_{SW} versus T and $B_{\parallel}$ and $B_{\perp}$).

TABLE I. Maximum values for T_{C}, B_{C} of Al, X1 and X2 as determined in Fig. 3. We take $T_{\mathrm{C,Al}}(B_{\mathrm{C}} = 0)$, $T_{\mathrm{C,X1}}(B_{\perp} = 50$ mT) and $B_{\mathrm{C}}(T \approx 0)$ to obtain their respective maximum values. The BCS superconducting gap is determined as $\Delta = 1.764 k_{\mathrm{B}} T_{\mathrm{C}}$ [45].

	T_{C} (K)	Δ (μV)	$B_{\mathrm{C}\star}$ (mT)	$B_{\mathrm{C}\perp}$ (mT)	$B_{\mathrm{C}\parallel}$ (mT)
Al	1.4±0.05	212±6	293± 10	41±2	282±10
X1	0.9±0.05	133±8	1230± 10	909±11	1010±20

	T_{C} (K)	Δ (μV)	$B_{\mathrm{C,Z}}$ (T)
X2	2.9±0.1	441±14	3.4±0.1

In Table. I we summarize the maximum T_{C}, the resulting superconducting gap Δ and B_{C} in the three field directions for Al and X1. Comparing $B_{\mathrm{C}\perp,\mathrm{Al}} = 41$ mT

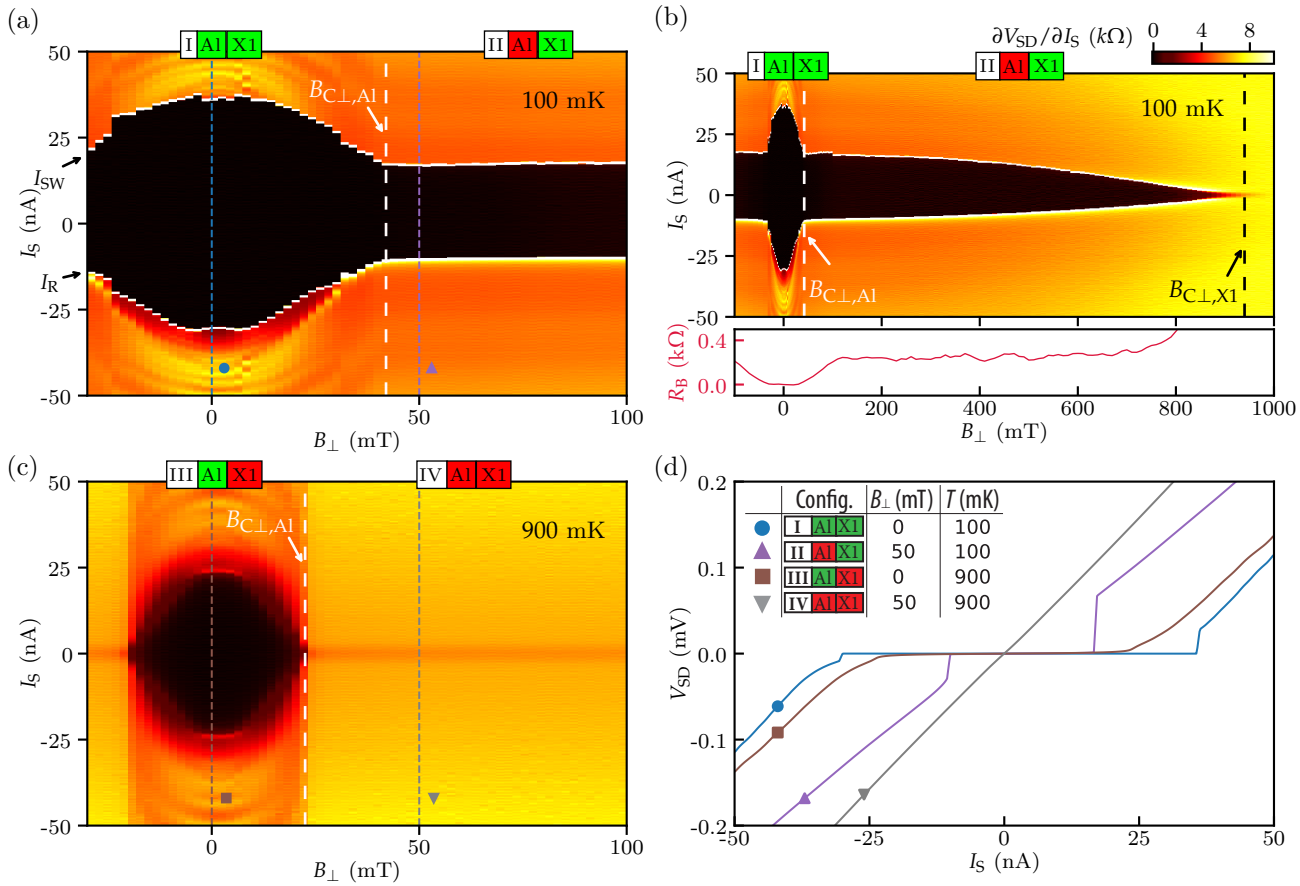

FIG. 2. **Device A: Josephson junction with two superconductors:** a) Differential resistance $\partial V_{SD}/\partial I_S$ versus I_S and $B_\perp$ taken at T = 100 mK. Black region corresponds to superconductivity. The white dashed line indicates $B_{C\perp,Al}$. Arrows indicate I_{SW} and I_R. b) Top panel: Same as a) for a larger range of $B_\perp$. The vertical black dashed line indicates $B_{C\perp,X1}$. Bottom panel: Horizontal cross-section showing $\partial V_{SD}/\partial I_S$ vs $B_\perp$ taken at I_S = 0. The color scale also applies to a) and b). c) Same as a) taken at T = 900 mK. d) Combinations of Al and X1 in the superconducting (green boxes) / normal (red boxes) state are numbered as configurations I-IV. Linecuts showing V_{SD} versus I_S taken for each configuration at the corresponding symbols in (a) and (c). Inset: table summarizing the configurations and values of $B_\perp$ and T for the respective linecuts. In all figures V_{BG} = −4.7 V and I_S is swept from negative to positive bias.

with $B_{C\star,Al}$ = 293 mT and $B_{C\parallel,Al}$ = 282 mT we notice a factor ~7 difference. This strong anisotropy for the out-of-plane field direction is clearly present in the $T_{C,Al}$-$B_{C,Al}$ curves in Fig. 3b and is expected for the large aspect ratio of the 50 nm thick Al contacts.

The $T_{C,X1}$-$B_{C,X1}$ curves show a less prominent magnetic field anisotropy from which we can roughly deduce the shape of X1 by assuming that the normal surface of the material is inversely proportional to the critical field, i. e., a larger superconducting normal-surface requires expelling more flux [45]. Using the respective ratios of $B_{C\star,X1}$, $B_{C\perp,X1}$ and $B_{C\parallel,X1}$ we observe that X1 is slightly elongated along the nanowire axis, reaffirming the hypothesis that X1 resides in the nanowire channel.

We now switch to the completely metalized device B where we believe Al has diffused completely through the channel, effectively making the nanowire a metallic superconductor. Fig. 3c shows I_{SW} vs T and B_Z where the corresponding $T_{C,X2}$-$B_{C,X2}$ relation in Fig. 3d is obtained by the previously mentioned polynomial fitting method. We see a critical temperature $T_{C,X2}$ = 2.9 K at B = 0 and critical field $B_{C,X2}$ = 3.4 T at T = 50 mK, both much higher than for X1 and the Al contacts. The switching current I_{SW} = 1.5 μA is two orders of magnitude higher compared to device A.

When comparing $T_{C,X2}$ = 2.9 K and $B_{C,X2}$ = 3.4 T with thin Al aluminium films [46], we observe X2 has equivalent properties of a ~ 3 nm thick film (in parallel field) and we could conclude that X2 is simply a very small cylinder of aluminium inside the nanowire channel. However, for X1 with $T_{C,X1}$ = 0.9 K and $B_{C,X1}$ ≈ 1 T an equivalent film thickness cannot be defined. Even though no inter-metallic phases were found for annealed pure Ge nanowires in Refs. 40, 41, a possible origin of X1 is the formation of a Al-Si/Ge alloy in our core-shell nanowires, albeit with a ratio of semiconductor to Al below that of

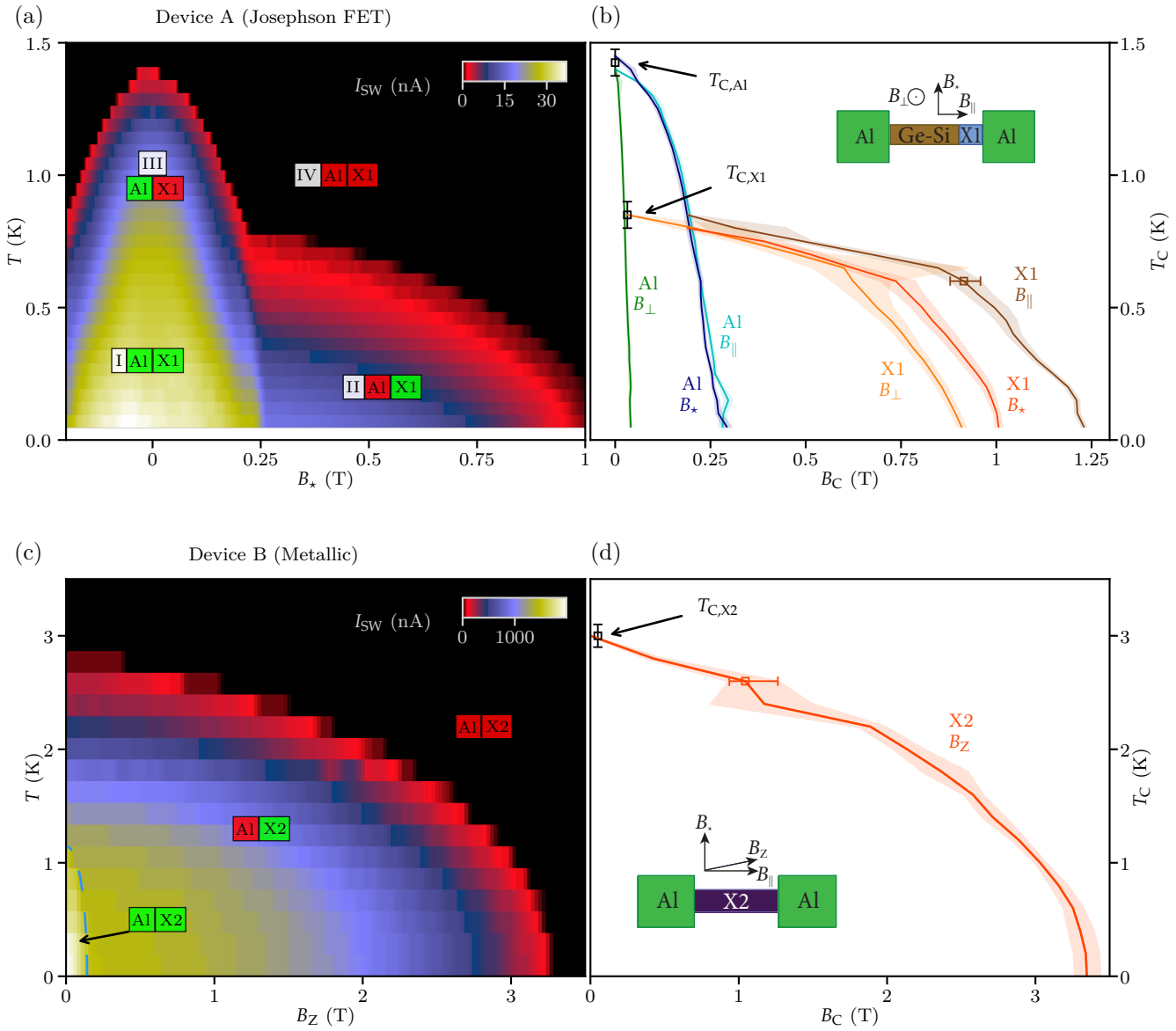

FIG. 3. **I_{SW}, T_C and B_C of a Josephson FET (device A) and a metallized nanowire device (device B):** a) I_{SW} versus T and $B_\star$ for the Josephson FET (device A). The green (red) boxes indicate whether the material is superconducting (normal) and show the configurations **I-IV** as defined in the main text. b) T_C vs B_C for Al and X1 for three main field axis $B_\perp$, $B_\parallel$ and $B_\star$ as illustrated by the inset. Curves are extracted from plots such as a) (see main text). c) I_{SW} versus T and B_Z for the completely metallized nanowire (device B) consisting of alloy X2. The green (red) boxes indicate three possible configurations. For the configuration where Al is superconducting (for B_Z < 300 mT and T < 1 K) an enhancement of I_{SW} can be observed as denoted by the blue dotted line. d) T_C vs B_C for X2 extracted from c). Inset shows the in-plane B_Z field direction which is rotated ~10° with respect to the nanowire. B_Z corresponds to the z-axis of the vector magnet, the only axis capable of fields > 1 T. In both b) and d), the vertical error bar represents an uncertainty in T_C of 2 % and shaded areas are standard deviations in B_C from fits.

our EDX detection limit. In literature, certain stoichiometric compositions indeed result in a lower T_C than for pure Al [47, 48] and in fact, one can get alloys with a T_C ranging from 0.5 K up to 11 K by various methods [49–53]. The exact composition of both X1 and X2 in our Ge-Si core-shell system therefore remains partly speculative and would require a more in-depth study like Ref. 41.

To sum up, we observe X1 with $T_{C,X1}$ = 0.9 K in a Josephson junction and X2 with $T_{C,X2}$ = 2.9 K in a metallic device, showing that diffusion of Al into Ge-Si nanowires can gives rise to different superconductors with a T_C lower and much higher than that of the Al contacts, both appear as a second superconductor in transport measurements.

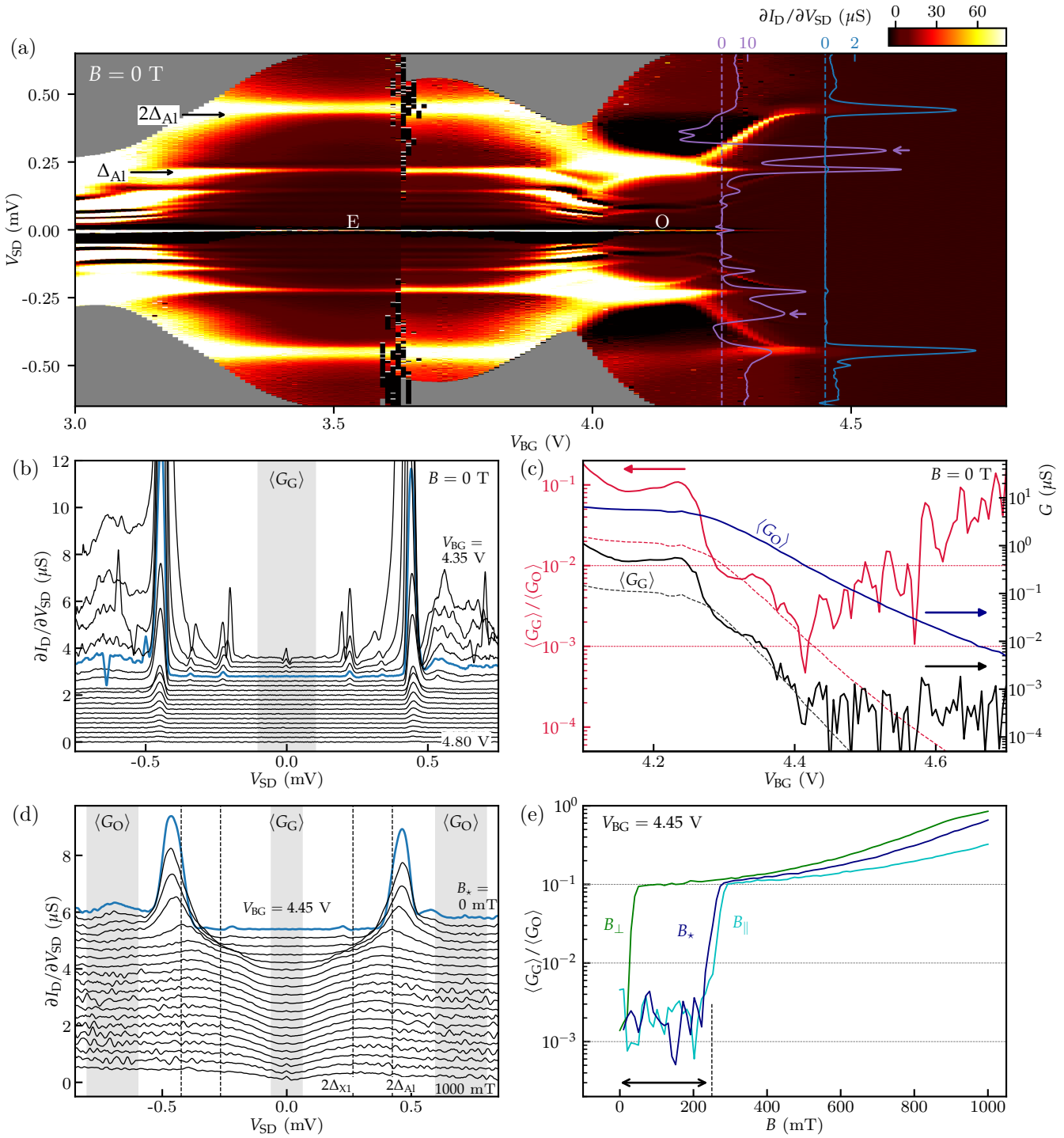

FIG. 4. **Hard superconducting gap in a Ge-Si nanowire Josephson FET (Device A):** a) Differential conductance $\partial I_D/\partial V_{SD}$ vs V_{SD} and V_{BG}. Odd (O) and even (E) hole occupation are denoted. The first two MAR orders are indicated at $V_{SD} = 2\Delta_{Al}$ and Δ_{Al}. b) Vertical linecuts from a) showing $\partial I_D/\partial V_{SD}$ vs V_{SD} at 50 mV intervals in V_{BG}, curves are offset by 0.2 μS. c) Averaged in-gap conductance $\langle G_G \rangle$ (black) and outside-gap conductance $\langle G_O \rangle$ (blue) and the ratio $\langle G_G \rangle / \langle G_O \rangle$ (red) versus V_{BG}. Dashed curves show theoretical minimal values and are the result of plotting Eq. (1). For every V_{BG}, $\langle G_G \rangle$ and $\langle G_O \rangle$ are averaged over a range of V_{SD} as indicated by the grey area in (b) and the grey dashed lines in Fig. SI-7 respectively. d) $\partial I_D/\partial V_{SD}$ vs V_{SD} for $B_\star$ from 0 to 1000 mT at 50 mT intervals. Curves are offset by 0.3 μS. Dashed lines show the expected position of the quasiparticle peak for $2\Delta_{Al}$ ($2\Delta_{X1}$) at $B = 0$. e) Ratio $\langle G_G \rangle / \langle G_O \rangle$ for the three main field axes $B_\perp$, $B_\parallel$ and $B_\star$ at $V_{BG} = 4.45$ V (blue line in (a), (b) and (c)). Ranges in V_{SD} where $\langle G_G \rangle$ and $\langle G_O \rangle$ are extracted are shown as grey areas in d).

TUNNELING REGIME OF THE JOSEPHSON FET

We now focus on device A and tune V_{BG} to a regime where the nanowire is near depletion. Fig. 4a shows the differential conductance $\partial I_{\mathrm{D}}/\partial V_{\mathrm{SD}}$ versus the source-drain voltage V_{SD} and the backgate voltage V_{BG}. We notice a zero-bias conductance peak as the result of a finite Josephson current and a prominent multiple Andreev reflection (MAR) pattern showing as horizontal lines of increased conductance for V_{BG} = 3 to 4 V. The reduced barrier transparency near depletion confines charges in the nanowire channel, and allows us to see odd and even charge occupation in a quantum dot in the wire [34] supported by a Kondo peak on the odd transitions [34, 54] (see Supplementary Information, Fig. S6). Above V_{BG} = 4.4 V, the MAR and zero-bias peak disappear, while the onset of quasiparticle transport is visible at the superconducting gap at $V_{\mathrm{SD}} = \pm 2\Delta_{\mathrm{Al}}$. This trend is also present in the $\partial I_{\mathrm{D}}/\partial V_{\mathrm{SD}}$ linecuts for V_{BG} between 4.35 and 4.80 V in Fig. 4b.

In Fig. 4a between V_{BG} = 4.2 V and V_{BG} = 4.4 V we observe a conductance peak in both bias directions smoothly moving from $|V_{\mathrm{SD}}| = \Delta_{\mathrm{AL}}$ to $|V_{\mathrm{SD}}| = 2\Delta_{\mathrm{AL}}$ when going from the odd to the even occupancy, which we attribute to an Andreev bound state (ABS). Additional evidence for an ABS presents itself in the form of a region of negative differential conductance in the odd occupancy between $V_{\mathrm{SD}} = \Delta_{\mathrm{AL}}$ and $V_{\mathrm{SD}} = 2\Delta_{\mathrm{AL}}$ [55, 56], as highlighted by the purple linecut at V_{BG} = 4.25 V in Fig. 3a. Tunnel spectroscopy on an ABS requires asymmetric opaque tunnel barriers where the most opaque barrier probes the ABS [54]. A barrier asymmetry in our devices can indeed be expected, since the final interface properties are determined by microscopic details on the Al-nanowire interface during annealing. For lower V_{BG} our barriers quickly become highly transparent [34] and we therefore only observe the ABS signature near depletion.

In contrast to the bias-symmetric MAR features, the asymmetric barriers show up in the intensity of the ABS signatures (see the arrows on the purple linecut in Fig. 4a). Depending on the bias direction, there are two different rate-determining tunnel sequences: (1) tunneling through an opaque barrier onto a single ABS or (2) tunneling from an ABS through an opaque barrier into the Fermi sea. Sequence (2) has a much higher tunnel probability than (1), which results in the observed asymmetry in conductance.

HARD SUPERCONDUCTING GAP

A measure for the amount of quasiparticle states inside the gap, is the in-gap suppression of conductance also termed as the hardness of the gap. We therefore investigate the ratio $\langle G_{\mathrm{G}}\rangle/\langle G_{\mathrm{O}}\rangle$ where $\langle G_{\mathrm{G}}\rangle$ ($\langle G_{\mathrm{O}}\rangle$) is a conductance value inside (outside) the gap averaged over a range of V_{SD} as shown in Fig. 4b. $\langle G_{\mathrm{O}}\rangle$ is determined from a similar measurement at higher bias (see Fig. SI-7), sufficiently far away from $2\Delta_{\mathrm{Al}}$. Fig. 4c shows $\langle G_{\mathrm{G}}\rangle$, $\langle G_{\mathrm{O}}\rangle$ and the ratio $\langle G_{\mathrm{G}}\rangle/\langle G_{\mathrm{O}}\rangle$ versus V_{BG} and we find the conductance is suppressed by a factor ~1000 for $V_{\mathrm{BG}} \approx 4.4$ V, an order of magnitude higher than previously reported in this system in the same superconductor-normal-superconductor (SNS) configuration [35].

A SNS junction can naively be viewed as two superconductor-normal (SN) junctions in series and the theoretical dependence of G_{G} on G_{O} can therefore be approximated as [57]:

$$G_{\mathrm{G,SNS}} \approx \frac{G_{\mathrm{G,SN}}}{2} = \frac{2e^2}{h}\frac{G_{\mathrm{O}}^2}{\left(\frac{4e^2}{h} - G_{\mathrm{O}}\right)^2}, \qquad (1)$$

and it follows that the equivalent conductance suppression of a SN device is a factor two lower than for a SNS device. We use the averaged $\langle G_{\mathrm{O}}\rangle$ as G_{O} and obtain the theoretical minimal in-gap conductance $G_{\mathrm{G,SNS}}$, as well as the corresponding ratio $G_{\mathrm{G,SNS}}/G_{\mathrm{O}}$, shown as dashed lines in Fig. 4c. We find that above V_{BG} = 4.25 V, the measured $\langle G_{\mathrm{G}}\rangle$ and $\langle G_{\mathrm{G}}\rangle/\langle G_{\mathrm{O}}\rangle$ closely follow the theoretical curves until the noise limit of our equipment is reached for $V_{\mathrm{BG}} > 4.4$ V. This suggests that $\langle G_{\mathrm{G}}\rangle$ is not dominated by quasiparticle poisoning and that our superconductor-semiconductor interfaces do not facilitate inelastic scattering and have low disorder [15]. We note that for these values of V_{BG}, the Ge-Si island is not fully depleted ($\langle G_{\mathrm{O}}\rangle$ still decreases as a function of V_{BG} and can be fully suppressed) and transport takes place through a tunnel-broadened quantum dot level (see also Ref. 34). However, the obtained theoretical minimal in-gap conductance should be considered an approximation since we do not take into account any difference in interface transparency between the two contacts.

When measured in a SNS configuration, the ratio $\langle G_{\mathrm{G}}\rangle/\langle G_{\mathrm{O}}\rangle$ gives an upper limit and could in reality be lower since it can be increased due to several other reasons than quasiparticle poisoning: (1) for higher V_{BG}, $\langle G_{\mathrm{G}}\rangle$ is limited by the noise floor of our measurement setup and does not further decrease. The decrease of $\langle G_{\mathrm{O}}\rangle$ now lowers the observed current suppression $\langle G_{\mathrm{G}}\rangle/\langle G_{\mathrm{O}}\rangle$. (2) For lower V_{BG}, MAR and the zero-bias peak, both characteristic for Josephson junctions, appear as conductance peaks inside the gap which leads to a decreased $\langle G_{\mathrm{G}}\rangle/\langle G_{\mathrm{O}}\rangle$ (3) The quantum dot in the junction may lead to Fabry-Perot resonances and Kondo-enhanced tunnelling around zero bias (see Fig. SI-6). SN devices will not exhibit these effects and may therefore result in a lower ratio $\langle G_{\mathrm{G}}\rangle/\langle G_{\mathrm{O}}\rangle$ and give a better approximation of the quasiparticle density in the gap. Because of this, we cannot directly compare the current

suppression in our device with other work probing the superconducting gap using a single superconducting contact. Nevertheless, the fact that our $\langle G_G \rangle / \langle G_O \rangle$ is limited by the noise floor our measurement setup suggests that our semiconductor-nanowire interface homogeneity could be comparable to InAs nanowire devices using epitaxial growth techniques [20] or specialized surface treatments [23].

We will now look at the magnetic field dependence of the hardness of the gap. We fix V_{BG} at 4.45 V and plot $\partial I_D / \partial V_{SD}$ versus V_{SD} for several $B_\star$ in Fig. 4d. For increasing $B_\star$, the sharp quasiparticle peak at $V_{SD} = 2\Delta_{Al}$ reduces in height and broadens up to $B_{C\star,Al} \approx 300$ mT. Above $B_{C\star,Al}$, we enter configuration **II** where only X1 is superconducting but which fails to produce a clear second quasiparticle peak at $\sim 2\Delta_{X1}$. Instead, we see a 'soft gap' signature [15] persisting up to $B_{C\star,X1}$ which we attribute to X1 having an ill-defined gap due to possible diffusion-induced spatial variations in its stoichiometry or geometry.

In Fig 4e we plot the ratio $\langle G_G \rangle / \langle G_O \rangle$ for the three main field directions. The initial ratio is $\sim 1 \cdot 10^{-3}$ in configuration **I** as defined in Fig. 2 and the gap remains hard until we approach the critical field of Al for the respective field direction as summarized in Table I (See Supplementary Information Fig. S8 for the corresponding differential conductance maps for all three main field axes). The highest field where the gap remains hard, $B_\parallel \approx 250$ mT, is slightly lower than $B_{C\parallel,Al}$ because of the strongly reduced Δ_{Al} at this field. The much softer gap in configuration **II** induced by X1 leads to a $\langle G_G \rangle / \langle G_O \rangle \approx 1 \cdot 10^{-1}$ which gradually increases to 1 approaching $B_{C,X1}$.

Another example of the change in transport properties when Al becomes normal is seen in Fig. 2a and Fig. 2c. Here, the fringes in the normal state attributed to multiple Andreev reflections (MAR) are only visible for $B_\perp < B_{C\perp,Al}$. For $B_\perp > B_{C\perp,Al}$, the absence of MAR suggests an increase of inelastic processes due to an ill-defined induced gap or a greatly increased quasiparticle poisoning rate.

The results in Fig. 4e show that the Al contacts needs to be superconducting in order to observe a hard gap. On the other hand, when only Al is superconducting, i. e., going from configuration **I** to **III** we observed no change in G_G that can be attributed to X1 becoming normal (see Supplementary Information, Fig. S9 for the temperature dependence of the differential conductance at $V_{BG} = 4.45$ V and $B = 0$). This suggests that X1 does not need to be a superconductor to observe a hard gap as long as the Al contacts proximise the entire junction. This is likely to happen, since the transparency between Al and X1 is high, and $\Delta_{Al} > \Delta_{X1}$ indicating a coherence length for X1 comparable or larger than for Al, i. e., in the order of μm [58].

Previously in this system a soft gap signature using NbTiN contacts has been shown [33], as well as hard gap using Al contacts [35]. This work adds an investigation of the superconductor-semiconductor interfaces and their microscopic properties. We therefore revisit Fig. 1b and c and take a closer look at the interface between the X1 and the Ge-Si island. Even though our TEM and EDX resolution prohibits a conclusive statements about the interface properties on an atomic scale, the abrupt change in contrast suggests an upper limit for the interface width of a few nanometer. As explained, this observation is supported by Refs. 40, 41 showing an atomically sharp interface between the Ge and Al segment where both remain crystalline [40, 41]. This type of interface would fit our observation of a hard gap, requiring a defect-free highly homogeneous heterointerface [15] and low junction transparency close to depletion. This indicates that the inter-diffusion reaction between Ge and Al is essential for the observed hard superconducting gap [40, 41].

Utilizing these interfaces in devices suitable for measuring Majorana fermions in this system [59] would require a high level of control over the inter-diffusion process, i.e., lateral diffusion and metalization of nanowire segments should be prevented. One route would be to perform device annealing while in-situ monitoring of the diffusion process as in Ref. 41, or possibly a higher level of control could be achieved by optimizing the annealing process. In addition, one would require thinner Al leads in order to withstand the required in-plane magnetic fields (> 1 T) to reach the topological phase transition [30, 38].

With a controlled inter-diffusion reaction, the superconductors X1 and X2 themselves would also pose as interesting materials since their high B_C in relation to their superconducting gaps, might allow the creation of Majorana fermions in materials where low g-factors could be limiting [60]. However, more research is required to understand the soft gap induced by X1 and to fully explore the possible superconductors, their composition, and formation process.

CONCLUSION

We have shown that Ge-Si nanowire devices with Al contacts contain additional superconductors after annealing, caused by diffusion of Al into the nanowire channel. We identify two superconductors in two different devices: X1 is present in a Josephson FET and X2 resides in a metallic nanowire channel. Both X1 and X2 remain superconducting for magnetic fields much higher than the Al contacts which could be of potential interest for applications where proximity-induced superconductivity is required in high magnetic fields.

Close to depletion, the Josephson FET exhibits a hard superconducting gap where the in-gap conductance is suppressed by a factor ~1000 in a SNS configuration where the in-gap conductance is close to the approximate

theoretical minimum. The gap remains hard up to magnetic fields of ~ 250 mT. For higher fields, a soft gap remains up to the critical field of X1. We can selectively switch Al or X1 from the normal to the superconducting state and, together with the TEM and EDX analysis, we believe that the diffusion-induced homogeneous heterointerface between the Ge core and the metalized nanowire segment is key in obtaining this hard gap. The next challenge is to more precisely control the diffusion of Al which would grant a highly promising system for observing Majorana zero modes [30].

ACKNOWLEDGEMENTS

The authors acknowledge financial support from the Netherlands Organization for Scientific Research (NWO). E.P.A.M.B. acknowledges financial support through the EC Seventh Framework Programme (FP7-ICT) initiative under Project SiSpin No. 323841. Solliance and the Dutch province of Noord-Brabant are acknowledged for funding the TEM facility. This project has received funding from the European Union's Horizon 2020 research and innovation programme under Grant Agreement #862046.

* Corresponding author, e-mail: f.a.zwanenburg@utwente.nl

[1] N. Read and D. Green, Physical Review B **61**, 10267 (2000).
[2] S. Das Sarma, M. Freedman, and C. Nayak, Physical Review Letters **94**, 166802 (2005).
[3] C. Nayak, S. H. Simon, A. Stern, M. Freedman, and S. Das Sarma, Reviews of Modern Physics **80**, 1083 (2008).
[4] A. Y. Kitaev, Physics-Uspekhi **44**, 131 (2001).
[5] Y. Oreg, G. Refael, and F. von Oppen, Physical Review Letters **105**, 177002 (2010).
[6] R. M. Lutchyn, J. D. Sau, and S. Das Sarma, Physical Review Letters **105**, 077001 (2010).
[7] R. M. Lutchyn, E. P. A. M. Bakkers, L. P. Kouwenhoven, P. Krogstrup, C. M. Marcus, and Y. Oreg, Nature Reviews Materials **3**, 52 (2018).
[8] A. Das, Y. Ronen, Y. Most, Y. Oreg, M. Heiblum, and H. Shtrikman, Nature Physics **8**, 887 (2012).
[9] V. Mourik, K. Zuo, S. M. Frolov, S. R. Plissard, E. P. A. M. Bakkers, and L. P. Kouwenhoven, Science **336**, 1003 (2012).
[10] M. T. Deng, C. L. Yu, G. Y. Huang, M. Larsson, P. Caroff, and H. Q. Xu, Nano Letters **12**, 6414 (2012).
[11] E. J. H. Lee, X. Jiang, R. Aguado, G. Katsaros, C. M. Lieber, and S. De Franceschi, Physical Review Letters **109**, 186802 (2012).
[12] A. D. K. Finck, D. J. Van Harlingen, P. K. Mohseni, K. Jung, and X. Li, Physical Review Letters **110**, 126406 (2013).
[13] H. O. H. Churchill, V. Fatemi, K. Grove-Rasmussen, M. T. Deng, P. Caroff, H. Q. Xu, and C. M. Marcus, Physical Review B **87**, 241401 (2013).
[14] M. T. Deng, C. L. Yu, G. Y. Huang, M. Larsson, P. Caroff, H. Q. Xu, P. Caroff, M. Larsson, G. Y. Huang, M. T. Deng, C. L. Yu, G. Y. Huang, M. Larsson, P. Caroff, and H. Q. Xu, Scientific Reports **4**, 7261 (2015).
[15] S. Takei, B. M. Fregoso, H. Y. Hui, A. M. Lobos, and S. Das Sarma, Physical Review Letters **110**, 186803 (2013).
[16] W. S. Cole, S. Das Sarma, and T. D. Stanescu, Physical Review B **92**, 174511 (2015).
[17] D. Rainis and D. Loss, Physical Review B - Condensed Matter and Materials Physics **85**, 1 (2012).
[18] A. P. Higginbotham, S. M. Albrecht, G. Kiršanskas, W. Chang, F. Kuemmeth, P. Krogstrup, T. S. Jespersen, J. Nygård, K. Flensberg, and C. M. Marcus, Nature Physics **11**, 1017 (2015).
[19] S. M. Albrecht, E. B. Hansen, A. P. Higginbotham, F. Kuemmeth, T. S. Jespersen, J. Nygård, P. Krogstrup, J. Danon, K. Flensberg, and C. M. Marcus, Physical Review Letters **118**, 137701 (2017).
[20] W. Chang, S. M. Albrecht, T. S. Jespersen, F. Kuemmeth, P. Krogstrup, J. Nygård, and C. M. Marcus, Nature Nanotechnology **10**, 232 (2015).
[21] M. Kjaergaard, F. Nichele, H. J. Suominen, M. P. Nowak, M. Wimmer, A. R. Akhmerov, J. A. Folk, K. Flensberg, J. Shabani, C. J. Palmstrøm, and C. M. Marcus, Nature Communications **7**, 12841 (2016).
[22] H. Zhang, Ö. Gül, S. Conesa-Boj, M. P. Nowak, M. Wimmer, K. Zuo, V. Mourik, F. K. de Vries, J. van Veen, M. W. A. de Moor, J. D. S. Bommer, D. J. van Woerkom, D. Car, S. R. Plissard, E. P. A. M. Bakkers, M. Quintero-Pérez, M. C. Cassidy, S. Koelling, S. Goswami, K. Watanabe, T. Taniguchi, and L. P. Kouwenhoven, Nature Communications **8**, 16025 (2017).
[23] Ö. Gül, H. Zhang, F. K. de Vries, J. van Veen, K. Zuo, V. Mourik, S. Conesa-Boj, M. P. Nowak, D. J. van Woerkom, M. Quintero-Pérez, M. C. Cassidy, A. Geresdi, S. Koelling, D. Car, S. R. Plissard, E. P. A. M. Bakkers, and L. P. Kouwenhoven, Nano Letters **17**, 2690 (2017).
[24] S. M. Albrecht, A. P. Higginbotham, M. Madsen, F. Kuemmeth, T. S. Jespersen, J. Nygård, P. Krogstrup, and C. M. Marcus, Nature **531**, 206 (2016).
[25] M. T. Deng, S. VaitiekÄŮnas, E. B. Hansen, J. Danon, M. Leijnse, K. Flensberg, J. Nygård, P. Krogstrup, and C. M. Marcus, Science **354**, 1557 (2016).
[26] Ö. Gül, H. Zhang, J. D. S. Bommer, M. W. A. de Moor, D. Car, S. R. Plissard, E. P. A. M. Bakkers, A. Geresdi, K. Watanabe, T. Taniguchi, and L. P. Kouwenhoven, Nature Nanotechnology **13**, 192 (2018).
[27] S. Conesa-Boj, A. Li, S. Koelling, M. Brauns, J. Ridderbos, T. T. Nguyen, M. A. Verheijen, P. M. Koenraad, F. A. Zwanenburg, and E. P. A. M. Bakkers, Nano Letters **17**, 2259 (2017).
[28] W. Lu, J. Xiang, B. P. Timko, Y. Wu, and C. M. Lieber, Proceedings of the National Academy of Sciences **102**, 10046 (2005).
[29] S. Zhang, F. J. Lopez, J. K. Hyun, and L. J. Lauhon, Nano letters **10**, 4483 (2010).
[30] F. Maier, J. Klinovaja, and D. Loss, Physical Review B **90**, 195421 (2014).

[31] M. Thakurathi, D. Loss, and J. Klinovaja, Physical Review B **95**, 155407 (2017).

[32] J. Xiang, A. Vidan, M. Tinkham, R. M. Westervelt, and C. M. Lieber, Nature Nanotechnology **1**, 208 (2006).

[33] Z. Su, A. Zarassi, B.-M. Nguyen, J. Yoo, S. A. Dayeh, and S. M. Frolov, arXiv:1610.03010 (2016).

[34] J. Ridderbos, M. Brauns, J. Shen, F. K. de Vries, A. Li, E. P. A. M. Bakkers, A. Brinkman, and F. A. Zwanenburg, Advanced Materials **30**, 1802257 (2018).

[35] F. K. de Vries, J. Shen, R. J. Skolasinski, M. P. Nowak, D. Varjas, L. Wang, M. Wimmer, J. Ridderbos, F. A. Zwanenburg, A. Li, S. Koelling, M. A. Verheijen, E. P. A. M. Bakkers, and L. P. Kouwenhoven, Nano Letters **18**, 6483 (2018).

[36] J. Ridderbos, M. Brauns, A. Li, E. P. A. M. Bakkers, A. Brinkman, W. G. van der Wiel, and F. A. Zwanenburg, Physical Review Materials **3**, 084803 (2019).

[37] C. Kloeffel, M. Trif, and D. Loss, Physical Review B **84**, 195314 (2011).

[38] F. Maier, C. Kloeffel, and D. Loss, Physical Review B **87**, 161305 (2013).

[39] M. Brauns, J. Ridderbos, A. Li, E. P. A. M. Bakkers, and F. A. Zwanenburg, Physical Review B **93**, 121408(R) (2016).

[40] S. Kral, C. Zeiner, M. Stöger-Pollach, E. Bertagnolli, M. I. den Hertog, M. Lopez-Haro, E. Robin, K. El Hajraoui, and A. Lugstein, Nano Letters **15**, 4783 (2015).

[41] K. El Hajraoui, M. A. Luong, E. Robin, F. Brunbauer, C. Zeiner, A. Lugstein, P. Gentile, J. L. Rouvière, and M. Den Hertog, Nano Letters **19**, 2897 (2019).

[42] W. F. Gale and T. C. Totemeier, *Smithells Metals Reference Book 8th edition*, edited by W. F. Gale. and T. C. Totemeier (Elsevier Ltd, 2003) p. 2080.

[43] P. Villars and K. Cenzual, eds., *Landolt-Börnstein - Group III Condensed Matter, Volume 43A11*, Landolt-Börnstein - Group III Condensed Matter, Vol. 43A11 (Springer Berlin Heidelberg, Berlin, Heidelberg, 2012).

[44] H. Courtois, M. Meschke, J. T. Peltonen, and J. P. Pekola, Physical Review Letters **101**, 1 (2008).

[45] M. Tinkham, *Introduction to Superconductivity Second Edition* (Dover Publications, Inc., Mineola, New York, 2004).

[46] R. Meservey and P. M. Tedrow, Journal of Applied Physics **42**, 51 (1971).

[47] G. Deutscher and M. Rappaport, Journal de Physique Lettres **40**, 219 (1979).

[48] J. Lesueur, L. Dumoulin, and P. Nédellec, Solid State Communications **66**, 723 (1988).

[49] G. Deutscher, J. Farges, F. Meunier, and P. Nedellec, Physics Letters A **35**, 265 (1971).

[50] C. C. Tsuei and W. L. Johnson, Physical Review B **9**, 4742 (1974).

[51] W. Kuan, S. Chen, S. Yi, Z. Wang, C. Wu, and P. Garoche, Journal of Low Temperature Physics **46**, 237 (1982).

[52] J. Chevrier, D. Pavuna, and F. Cyrot-Lackmann, Physical Review B **36**, 9115 (1987).

[53] X.-X. Xi, Q.-Z. Ran, J.-R. Liu, and W.-Y. Guan, Solid State Communications **61**, 791 (1987).

[54] B.-K. Kim, Y.-H. Ahn, J.-J. Kim, M.-S. Choi, M.-H. Bae, K. Kang, J. S. Lim, R. López, and N. Kim, Physical Review Letters **110**, 076803 (2013).

[55] J.-D. Pillet, C. H. L. Quay, P. Morfin, C. Bena, A. L. Yeyati, and P. Joyez, Nature Physics **6**, 965 (2010).

[56] J. Gramich, A. Baumgartner, and C. Schönenberger, Physical Review B **96**, 1 (2017).

[57] C. W. J. Beenakker, Physical Review B **46**, 12841 (1992).

[58] R. Gross and A. Marx, *Applied superconductivity,*, Vol. 1 (2005) p. 480.

[59] F. Maier, T. Meng, and D. Loss, Physical Review B **90**, 155437 (2014).

[60] T. D. Stanescu and S. Tewari, Journal of Physics: Condensed Matter **25**, 233201 (2013).

Supporting Information: Hard superconducting gap and diffusion-induced superconductors in Ge-Si nanowires

FABRICATION

Ge-Si core-shell nanowires are deposited on a p^{++} doped Si substrate covered with 100 nm SiO_2 and contacted after AFM imaging. Source and drain contacts are defined using electron-beam lithograph and after developing, a 3 second buffered hydrofluoric acid (12.5 %) dip is performed to remove native SiO_2 from the Si shell of the nanowire. The contacts are metallized using electron-beam evaporation of Al, resulting in a 150 nm nanowire channel. As a last step, devices are annealed for 10 minutes on a hotplate in ambient at 180°C during which Al diffuses into the wire. As a result, a drop in room temperature resistance from several MΩ to several kΩ was observed for ~ 80 % of devices.

In total, 7 out of 15 devices tested at low temperature showed a supercurrent with 4 devices showing a superconducting phase with a T_C between 600 and 900 mK, comparable to X1. Three devices showed a metallized nanowire with comparable I_{SW} to device B, we have no information on their respective T_C or B_C.

EXTRACTION OF T_C-$B_{C\star}$ CURVES

Here we explain how the T_C-$B_{C\star}$ curves of Fig. 3b in the main text were generated. We define $B_{C\star,Al}$ ($B_{C\star,X1}$) as the field where Al (X1) no longer induces a supercurrent, i. e., we no longer observe a I_{SW}. In Fig. 3a we cannot directly observe $B_{C\star,Al}$ for $0 < T < 800$ mK where the 'peak' of Al and the 'tail' of X1 overlap (for $230 < B_\star < 300$ mT) and we therefore use the following method: (1) For all temperatures we take each individual I_{SW}-$B_\star$ curve, i. e., horizontal linecuts in Fig.3a, (2) we select only I_{SW} where $B_\star < B_{C\star,Al}$ (3) we fit I_{SW} to an empirical polynomial of the form $I_{SW}(B_\star) = aB_\star^4 + bB_\star^2 + c$ with a and b only allowed negative while c is always positive, (4) we find $B_{C\star,Al}$ for each temperature as the roots of $I_{SW}(B_\star)$ (i. e., zero crossings). For X1 we use the same method except in (2) we select only I_{SW} for $B_\star > B_{C\star,Al}$.

ADDITIONAL FIGURES AND TABLES

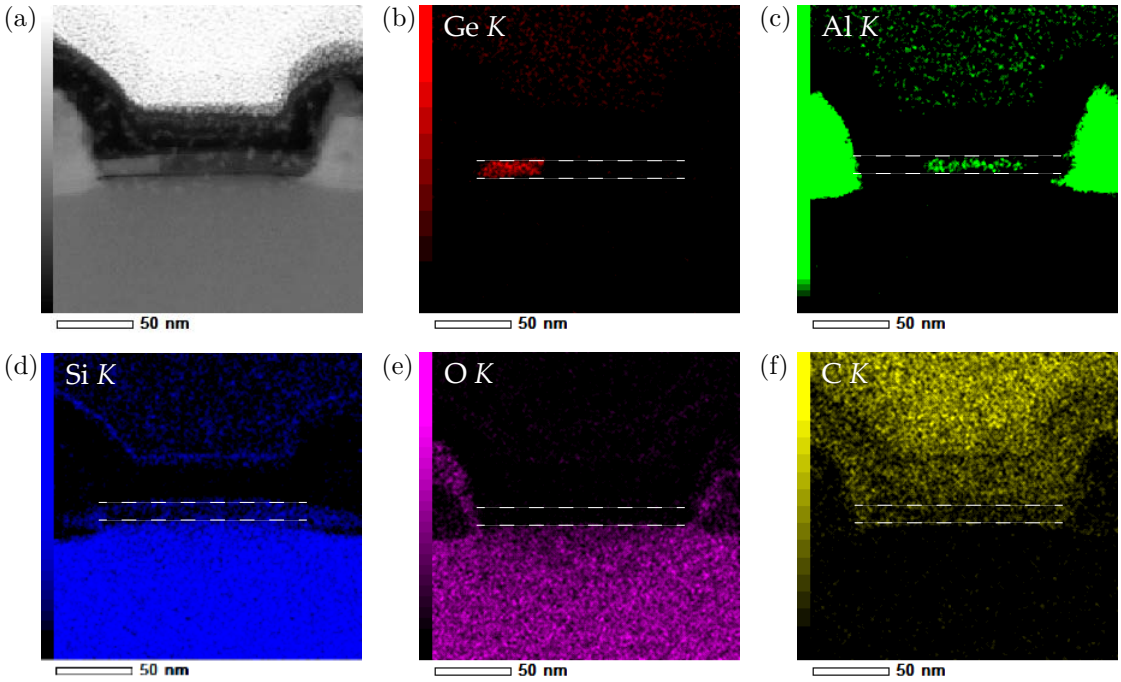

FIG. S1. **EDX maps of various elements of device A:** a) TEM image of device A, same as Fig.1b in the main text. EDX map for Ge (b), Al (c), Si (d), O (e) and C (f). White dashed lines indicate the approximate position of the nanowire. (a), (b), (c) and (d) were used to construct Fig.1c in the main text.

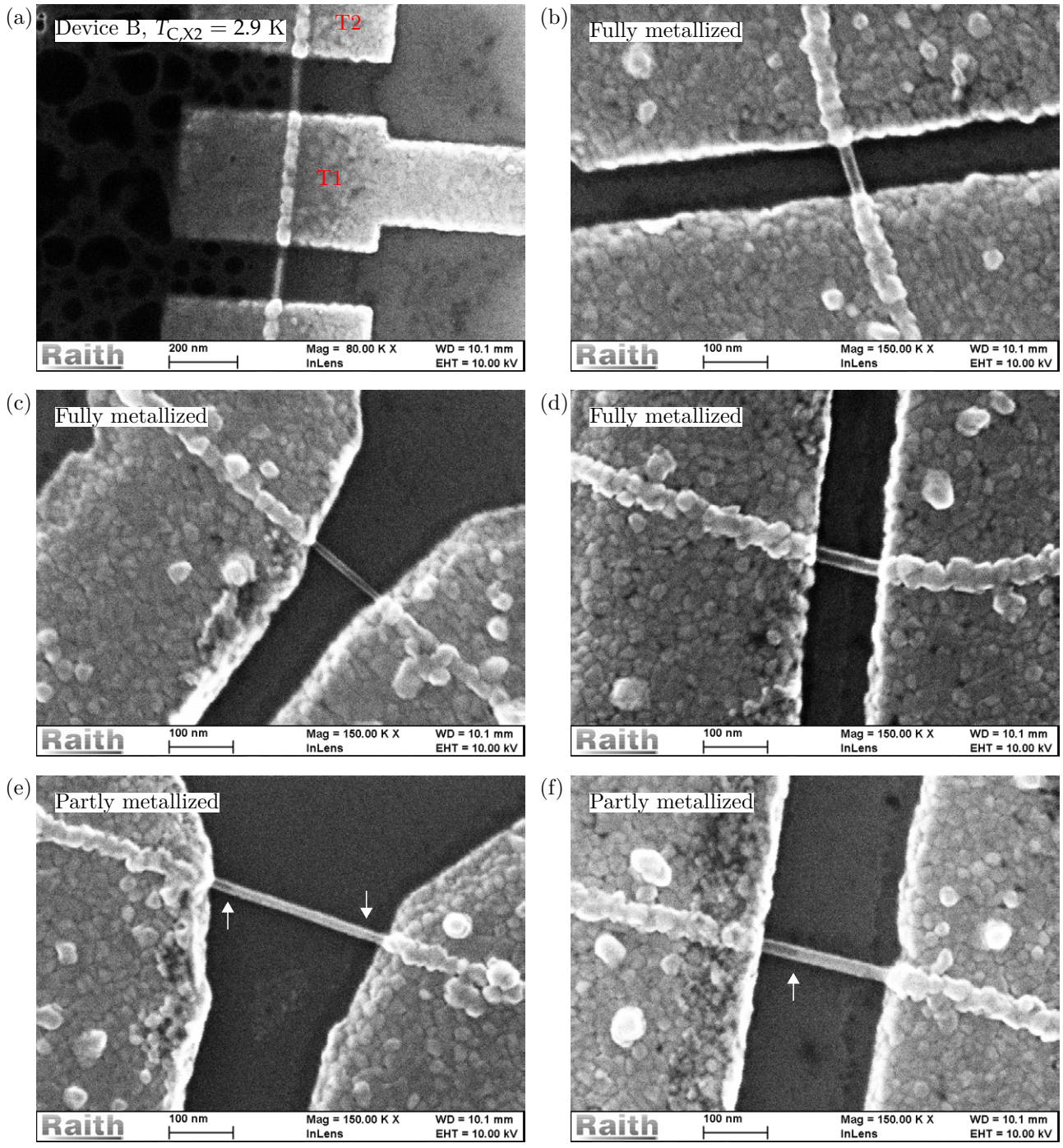

FIG. S2. **SEM images of devices:** All devices have undergone the same annealing process. a) SEM image of device B. Carbon contamination prevents a conclusive analysis of the Al-Ge inter-diffusion process. We suspect that the metallized nanowire segment is located between T1 and T2 based on the low contrast of the nanowire segment. b) Another metallized device exhibiting the same darkened color in the nanowire segment as in a), no additional superconducting phase was found in this device. c), d) More devices where the complete channel shows a low contrast for which we suspect they are fully metallized. e), f) Devices with a region of lower contrast close to the Al contacts, suspected due to partial metalization with the white arrows denoting the Al-Ge inter-diffusion front. Devices c) - f) were not measured. Other devices that were measured could not be imaged afterwards.

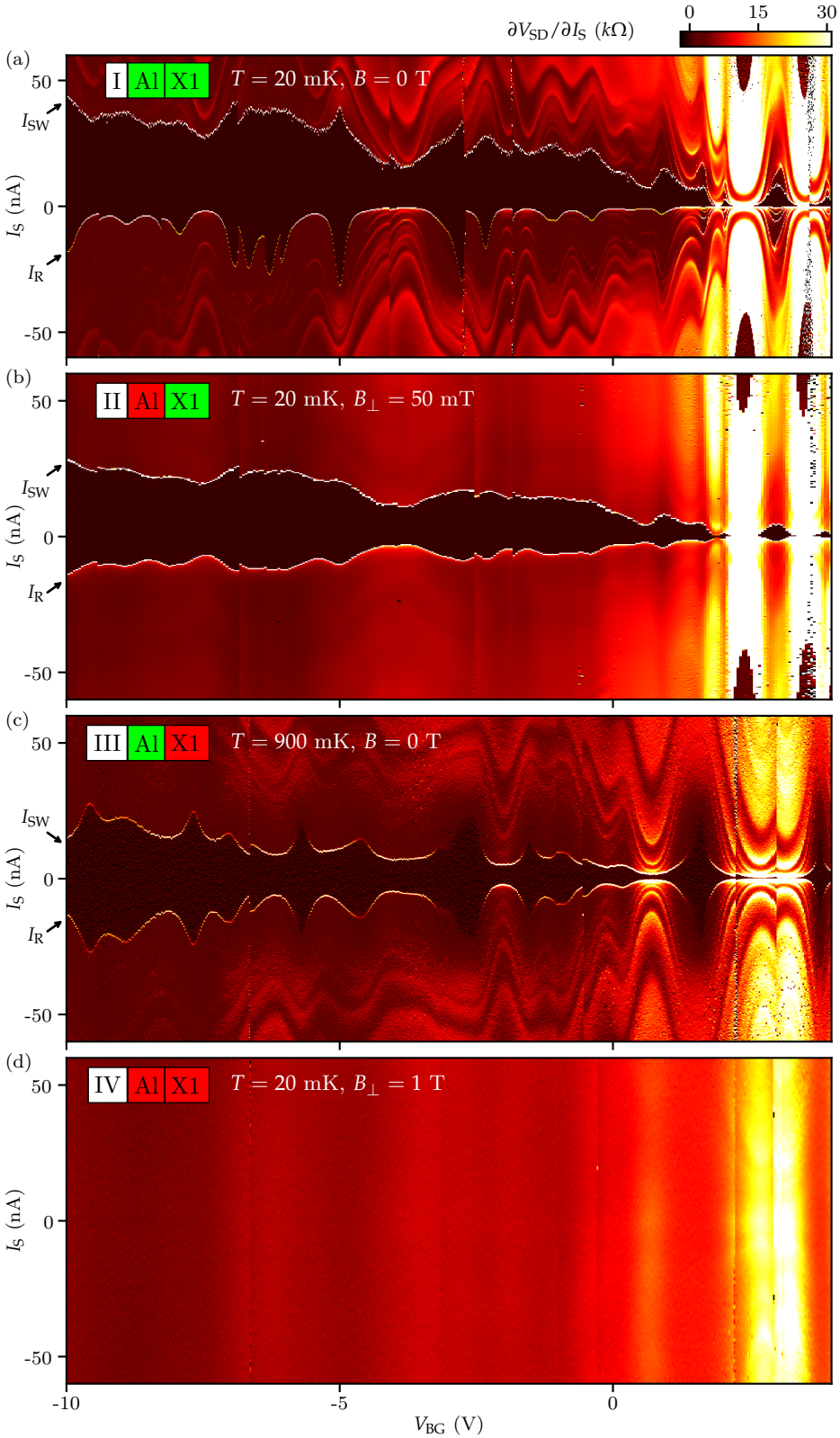

FIG. S3. **Backgate dependence for all four configurations:** All figures show $\partial V_{SD}/\partial I_S$ vs I_S and V_{BG} with I_S measured from negative towards positive bias. a) Configuration **I** taken at T = 20 mK and B = 0 T. b) Configuration **II** taken at T = 20 mK and $B_\perp$ = 50 mT. c) Configuration **III** taken at T = 900 mK and B = 0 T. d) Configuration **IV** taken at T = 20 mK and $B_\perp$ = 1 T. In all figures, I_S was swept from negative to positive bias during measurement. a), b) and d) were taken during the same cooldown, all figures share the same color scale displayed in a). In a), b) and c), I_{SW} and I_R are denoted.

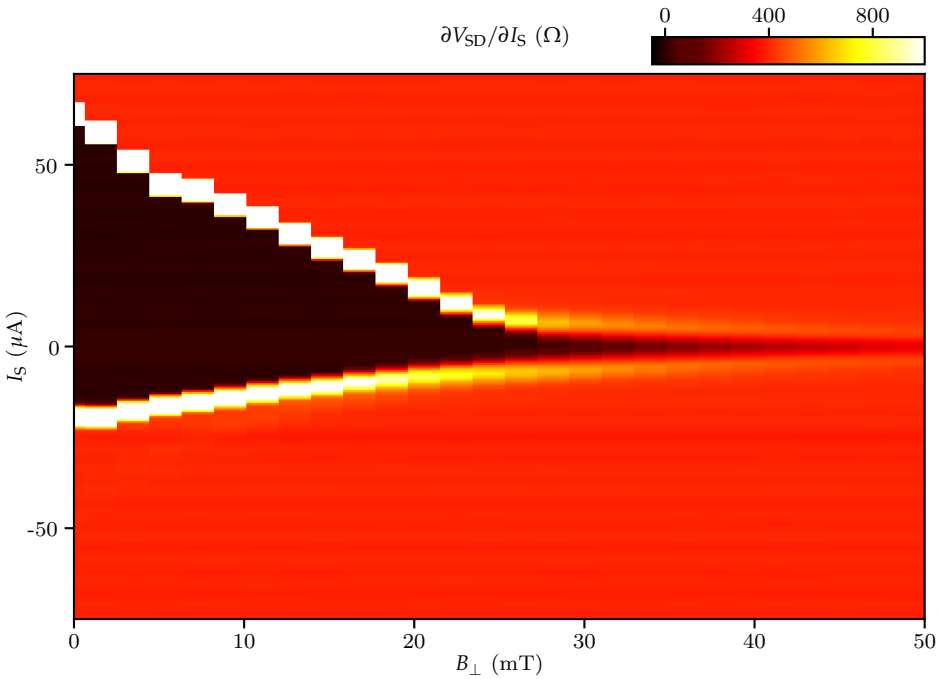

FIG. S4. **Al lead in an out-of-plane field:** $\partial V_{SD}/\partial I_S$ vs I_S and $B_\perp$. The Al lead has a thickness of ~ 50 nm and I_{SW} is determined by its smallest width of ~ 500 nm running over a length of several μm. The black region denotes a supercurrent. The lead is measured in a 2-probe configuration and a series resistance of two times the line resistance is subtracted. Measurements are taken in the positive bias direction where the asymmetry in bias is attributed to local Joule heating.

TABLE S1. Configurations of device A with two superconducting phases and the corresponding conditions for the magnetic field **B** and temperature **T**, SC refers to superconductivity. The last column refers to the plots in Fig.2d. For generality the field direction is removed from the subscripts.

Configuration	Superconducting	Normal state	Conditions	I_{SW} and symbol
I	Al,X1		$\mathbf{B} < B_{C,Al}, B_{C,X1}$ & $\mathbf{T} < T_{C,X1}, T_{C,Al}$	$I_{SW} \approx 36$ nA ●
II	X1	Al	$B_{C,Al} < \mathbf{B} < B_{C,X1}$ & $\mathbf{T} < T_{C,X1}, T_{C,Al}$	$I_{SW} \approx 17$ nA ▲
III	Al	X1	$\mathbf{B} < B_{C,Al}, B_{C,X1}$ & $T_{C,X1} < \mathbf{T} < T_{C,Al}$	$I_{SW} \approx 24$ nA ■
IV		Al,X1	$\mathbf{B} > B_{C,X1}$ or $\mathbf{T} > T_{C,Al}$ or $B_{C,Al} < \mathbf{B} < B_{C,X1}$ & $T_{C,X1} < \mathbf{T} < T_{C,Al}$	$I_{SW} = 0$ ▼

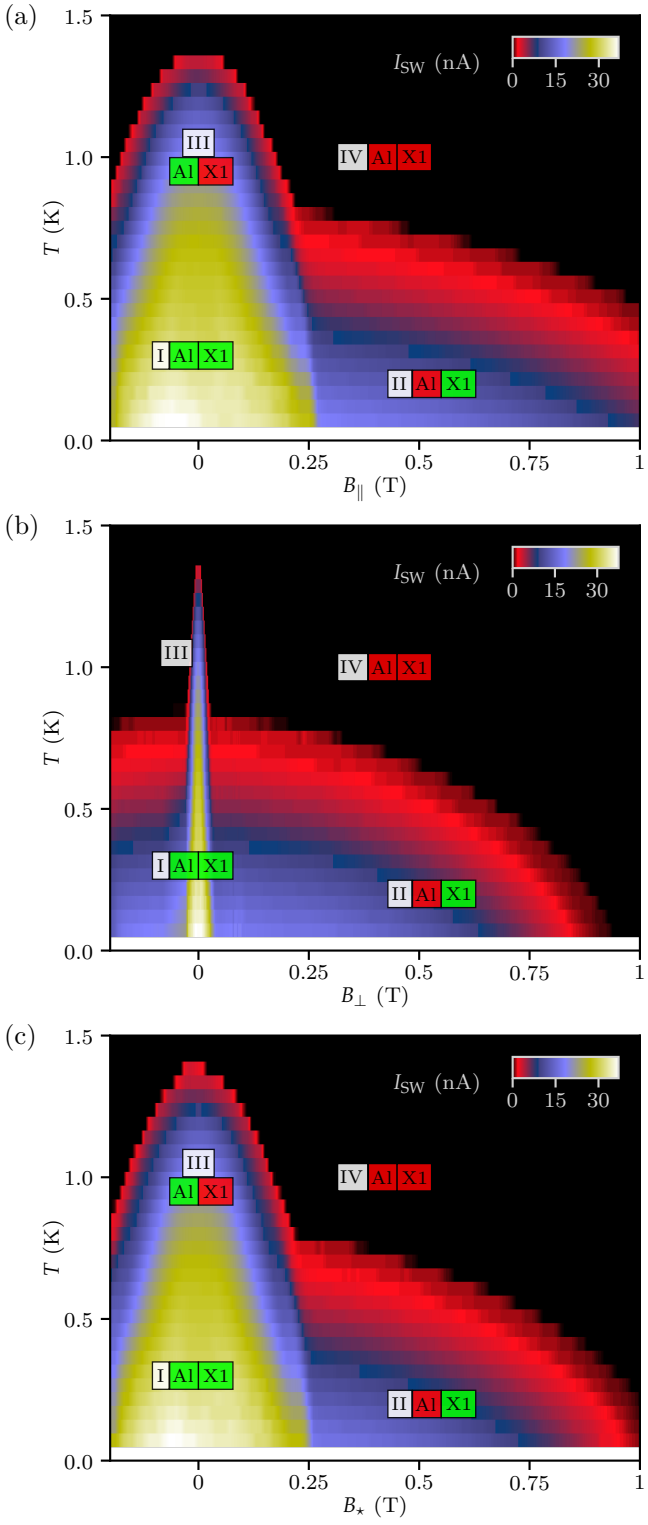

FIG. S5. **I_{SW} vs T and B of Device A:** Datasets were used to generate Fig.3b in the main text as explained in section SII. a) I_{SW} vs $B_{\parallel}$ and T, b) I_{SW} vs $B_{\perp}$ and T and c) I_{SW} vs $B_{\star}$ vs T (same as Fig.3a in the main text). Configuration I-IV are denoted in all figures in which green indicates superconductivity while red indicates the normal state.

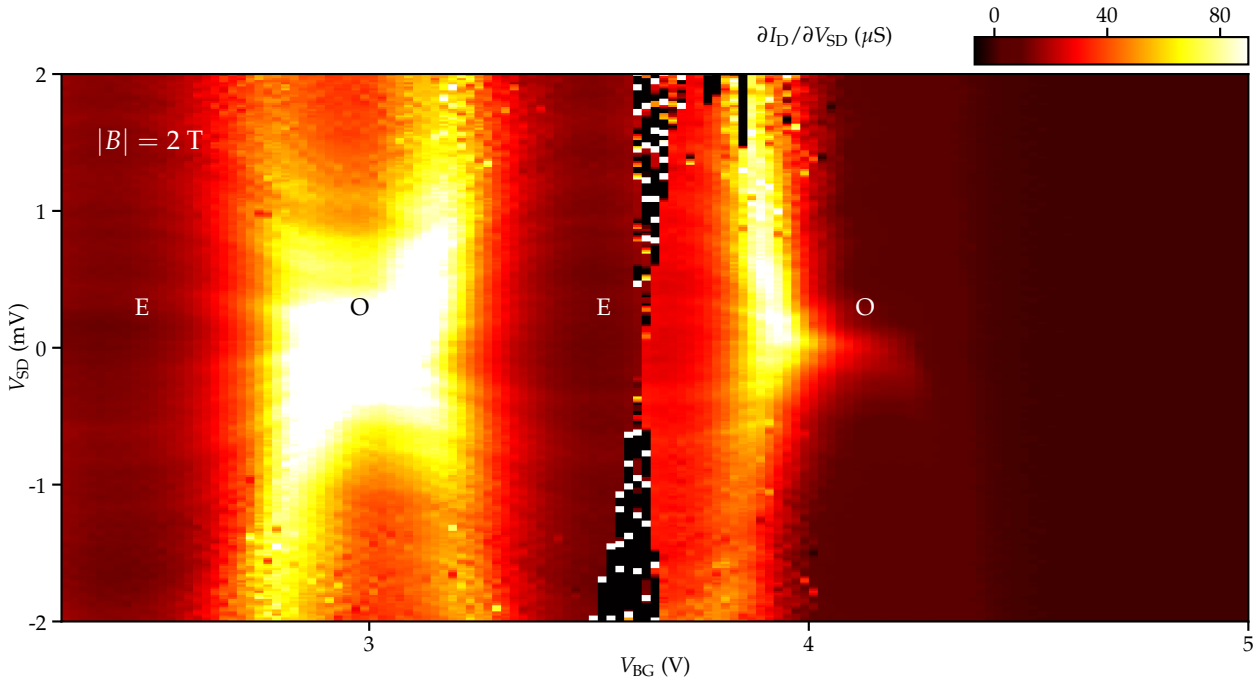

FIG. S6. **Kondo effect at finite magnetic field:** $\partial I_D/\partial V_{SD}$ vs V_{SD} and V_{BG} for $|B|$ = 2 T. Odd (O) and even (E) hole occupation of the nanowire quantum dot is indicated. The Kondo effect is visible for odd occupation as increased conductance around V_{SD} = 0.

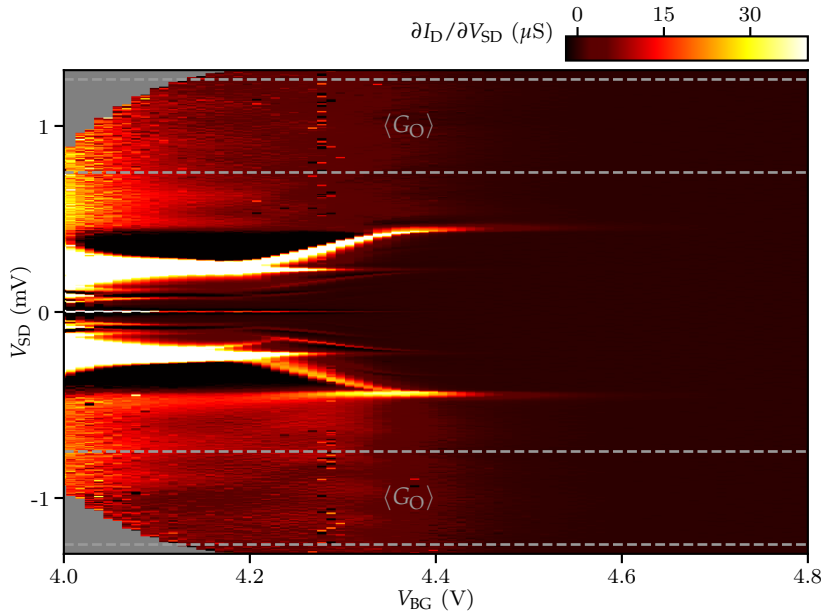

FIG. S7. **Determination of $\langle G_O \rangle$:** $\langle G_O \rangle$ is determined from this dataset measured at higher bias compared to the dataset shown in Fig.4a in the main text. $\langle G_O \rangle$ is determined as the averaged conductance over a range V_{SD} delimited by the dashed grey lines. Conductance values for positive and negative bias are used. A correction to their corresponding values of V_{BG} is applied to compensate for the gate lever arm $\alpha \approx 0.18$ (see Ref.[34] in the main text).

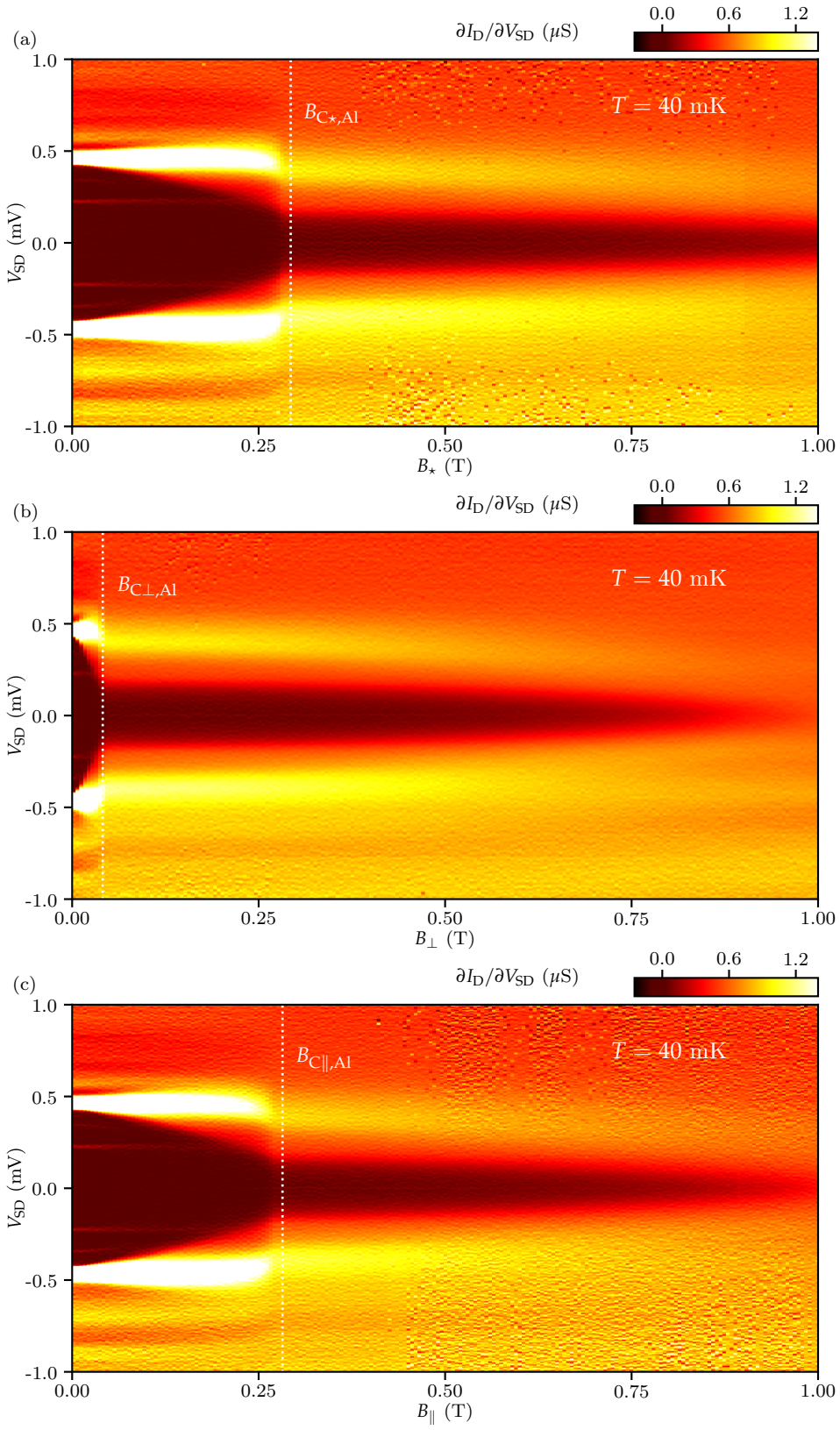

FIG. S8. **Superconducting gap versus B:** Datasets used to generate Fig.4d and Fig.4e in the main text, taken at V_{BG} = 4.45 (blue dotted line in Fig.a. a) $\partial I_D/\partial V_{SD}$ vs V_{SD} and $B_\star$, the white dotted line indicates the critical field of Al $B_{C\star,Al}$. b) $\partial I_D/\partial V_{SD}$ vs V_{SD} and $B_\perp$, the white dotted line indicates $B_{C\perp,Al}$. c) $\partial I_D/\partial V_{SD}$ vs V_{SD} and $B_\parallel$, the white dotted line indicates $B_{C\parallel,Al}$. Faint zero-bias peaks attributed to the Kondo effect appear only above $B_{C\star,Al}$.

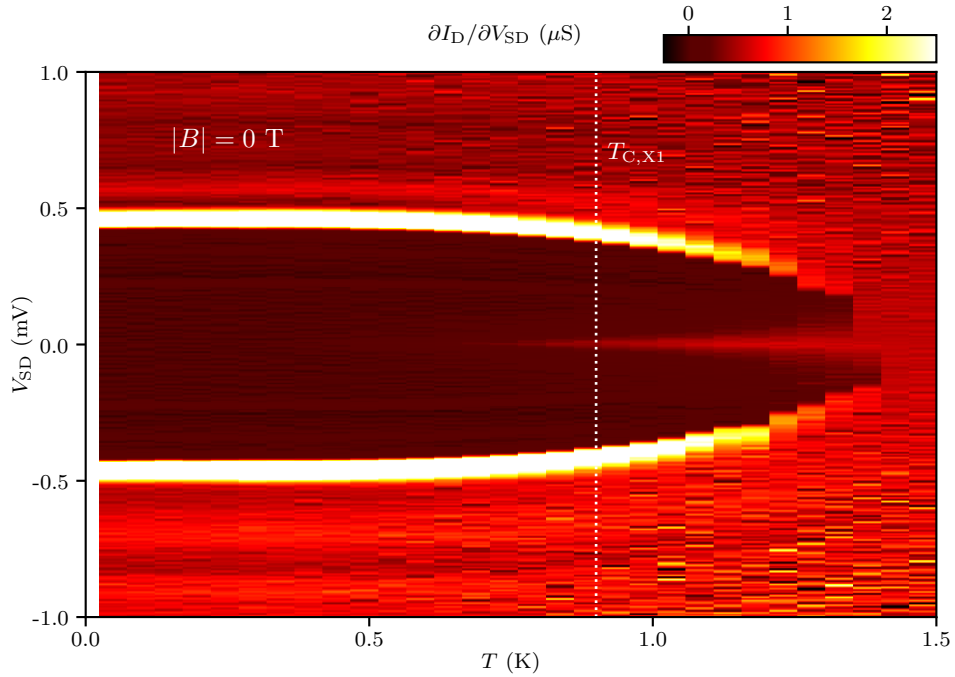

FIG. S9. **Superconducting gap versus T:** $\partial I_D/\partial V_{SD}$ vs V_{SD} and T taken at V_{BG} = 4.45 (blue dotted line in Fig.4a). The white dotted line indicates the critical temperature of X1 $T_{C,X1}$. No abrubt change in conductance is observed above $T_{C,X1}$.